

1       **Triggering effects of large topography and boundary layer turbulence on**  
2       **convection over the Tibetan Plateau**

3       **Xiangde Xu<sup>1</sup>, Yi Tang<sup>1,2</sup>, Yinjun Wang<sup>1</sup>, Hongshen Zhang<sup>3</sup>, Ruixia Liu<sup>4</sup> and**  
4       **Mingyu Zhou<sup>5</sup>**

5

6       <sup>1</sup> State Key Laboratory of Severe Weather, Chinese Academy of Meteorological  
7       Sciences, Beijing, China.

8       <sup>2</sup> School of Environmental Studies, China University of Geosciences, Wuhan, China.

9       <sup>3</sup> Peking University, Beijing, China

10      <sup>4</sup> CMA Earth System Modeling and Prediction Centre (CEMC), Beijing, China

11      <sup>5</sup> National Marine Environmental Forecasting Center, Beijing, China

12

13      Corresponding author: Yinjun Wang (pbl\_wyj@sina.cn) and Hongshen Zhang  
14      (hsdq@pku.edu.cn)

15      **Abstract**

16      In this study, we analyze the diurnal variations and formation mechanism of low  
17      clouds at different elevations. We further discuss whether there exists s triggering  
18      mechanism for convection over the Tibetan Plateau (TP), and whether there is an  
19      association among low air density, strong turbulence and ubiquitous “popcorn-like”  
20      cumulus clouds. The buoyancy term (BT) and shear term (ST) over the TP are  
21      significantly greater than those at the low elevation, which is favorable for the  
22      formation of increasing planetary boundary layer height (PBLH), and also plays a key  
23      role in the convective activities in the lower troposphere. The lifting condensation  
24      level (LCL) increases with the increasing of PBLH-LCL over the TP. From the  
25      viewpoint of global effects, the triggering effects of the dynamical structure within the  
26      boundary layer on convective clouds in the Northern Hemisphere are analyzed. There  
27      are strong ST and BT at two high elevation regions (TP and Rocky Mountains), and  
28      the strong thermal turbulence results in obvious positive value of PBLH-LCL at high  
29      elevation regions under low RH condition in the Northern Hemisphere. The values of  
30      PBLH-LCL slightly greater than zero correspond spatially to moreincreased low  
31      cloud cover (LCC) in the central part of Rocky Mountains, but the obvious large-scale  
32      subsidence on both sides of the mountain leads to strong inversion above PBL and  
33      lower RH in PBL, which further lead to lessdecreased LCC in these areas. Thus less  
34      LCC is generated at Rocky Mountains compared to the TP.

35 **Introduction**

36 The Tibetan Plateau (TP), which resembles a "third pole" and a "world water  
37 tower", plays an important and special role in the global climate and energy–water  
38 cycle (Xu et al., 2008; Wu et al., 2015). The TP covers a quarter of China.  
39 Additionally, the average altitude of the TP is 4000 meters, reaching 1/3 of the  
40 tropopause height, so it is called the "World Roof". Cumulus convection over the TP  
41 transfers heat, moisture and momentum into the free troposphere, which can impact  
42 the atmospheric circulation regionally and globally (Li and Zhang, 2016; Xu et al.,  
43 2014) and reveals the important "window effect" for the transfer and exchange of  
44 global energy and water vapor over the TP. The It is the dynamic effect from the  
45 special heat source—dynamic effect that constitutes the "window effect" and  
46 "thermally driven" mechanism over the TP.

47 The results of the second Tibetan Plateau Experiments (TIPEX II), which ~~was~~<sup>were</sup>  
48 carried out in 1998, showed that the strong convective plumes within PBL observed  
49 by sodar and a frequently occurred deep mixed layer (>2 km) can lead to ubiquitous  
50 "popcorn-like" cumulus clouds in Dangxiong, as proposed by Zhou et al. (2000)~~in~~  
51 Dangxiong, and Xu et al. (2002) proposed~~came up with~~ a comprehensive physical  
52 pattern of land-air dynamic and thermal structure on the Qinghai-Xizang Plateau~~TP~~  
53 (Xu et al., 2002; Zhou, 2000). The previous studies have done many valuable  
54 researches on the triggering mechanism of moist convection over moist and dry  
55 surfaces based on atmospheric observations and simulations (Ek and Mahrt, 1994;  
56 Findell and Eltahir, 2003; Gentine et al., 2013). For dry surface, the weak  
57 stratification and strong sensible heat flux result in the rapid growth of PBLH so that  
58 the relative humidity at the top of the boundary layer  $RH_{top}$  increases rapidly, which  
59 favors the formation of clouds. For moist surface, strong stratification and evaporation  
60 (small bowen ratio) not only result in~~cause~~ slow growth of PBLH, ~~but~~<sup>also</sup> increase  
61 the mixed layer specific humidity and  $RH_{top}$ , which favor the formation and  
62 development of clouds. Taylor et al. (2012) found that the afternoon rain falls  
63 preferentially over soils that are relatively dry compared to the surrounding area,  
64 especially for semi-arid regions. Guillod et al. (2015) reconciled spatial and temporal  
65 soil moisture effects on the afternoon rainfall. They showed that afternoon  
66 precipitation events tend to occur during wet and heterogeneous soil moisture  
67 conditions, while being located over comparatively drier patches. Tuttle et al. (2016)  
68 showed the empirical evidence of contrasting soil moisture–precipitation feedbacks  
69 across the United States, and they found that soil moisture anomalies significantly  
70 influence rainfall probabilities over 38% of the area with a median factor of 13%.  
71 Findell et al. (2003) analyzed~~According to~~ the model results over dry and wet soils in  
72 Illinois, Findell et al. (2003) Then~~t~~They summarized the predictive capability of rain  
73 and shallow clouds gained from use~~by~~ using of the convective triggering potential  
74 (CTP) and a low-level humidity index, with  $HI_{low}$  as measures of the early morning  
75 atmospheric setting. Our previous studies pointed out that the developments of these

76 cumulus clouds are related to the special large scale dynamic structure and turbulence  
77 within PBL over the TP (Xu et al., 2014; Wang et al., 2020). In addition, Wang et al.,  
78 (2020) pointed out that, despite the same relative humidity between eastern China and  
79 the TP, the lower temperature over the TP results in a lower lifting condensation level.  
80 With the same surface sensible heat flux, lower air density over the TP results in a  
81 larger buoyancy flux and a deeper boundary layer. All the above results indicate the  
82 topography of the TP plays a major role in increasing the occurrence frequency of the  
83 strong convective clouds (Luo et al., 2011). This conclusion is consistent with the  
84 viewpoint of Flohn (1967) who emphasized the chimney effect of the huge  
85 cumulonimbus clouds on heat transfer in the upper troposphere.

86 The TP is one of the regions in China where that is featured with high frequency  
87 of cumulus clouds ~~occurs~~, and the development of cumulus system is related to both  
88 the turbulence and special dynamical structure in PBL over the TP. The vertical  
89 motion over the TP is associated with the anomalous convective activities. However,  
90 as Li and Zhang (2016) mentioned, the details of PBL process are not very clear, ~~and~~  
91 ~~also~~. The same is true for the diurnal variations and formation mechanism of low  
92 clouds over the TP and low elevation regions ~~are still not very clear~~. The different  
93 variation characteristics of these low clouds at different elevations and regions also  
94 need to be discussed and analyzed. Moreover, We further need to discuss investigate  
95 whether there exist “high efficiency” triggering mechanisms for convection over the  
96 TP, and whether there is an association among low air density, strong turbulence and  
97 ubiquitous “popcorn-like” cumulus clouds. Is there also strong turbulence at higher  
98 elevation regions with lower air density in the globe? What is the impact of the large  
99 scale vertical motions on clouds? Because both the TP and Rocky Mountains are high  
100 elevation regions ~~with huge covering large area in mid-latitude areas~~, in this study we  
101 mainly focus on these two regions to analyze the above scientific questions.

## 102 2 Observational and reanalysis data

103 We use in situ measurements of temperature (T) and relative humidity (RH) at 2 m  
104 height, surface pressure data every hour, and low cloud cover (LCC) every three  
105 hours from 2402 automatic weather stations— from June to August of 2010-2019 in  
106 China. LCC here refers to the fraction of the sky covered by low clouds as estimated  
107 by human observers, including five cloud types: nimbostratus (Ns), stratocumulus  
108 (Sc), stratus (St), cumulus (Cu), and deep convection (DC). These surface observation  
109 datasets are provided by China National Meteorological Information Center.

110 In addition, we use the hourly  $0.25^\circ \times 0.25^\circ$  ERA5 reanalysis surface-layer data  
111 in summer (June 1 to August 31) from 2010 to 2019 (Hersbach et al., 2020).

112 We use more than 4 years (from June 15 2006 to August 31 2010) of the satellite  
113 (CloudSat radar and Calipso lidar)-merged cloud classification product  
114 2B-CLDCLASS-lidar to calculate the mean LCC with  $1^\circ \times 1^\circ$  resolution at about 2:00  
115 pm and 2:00 am LT in summer. The introduction of this product and details of the  
116 LCC calculation methods are summarized in Sassen and Wang (2008) and Wang et al  
117 (2020).

118 We use a Gaofen 4 (GF 4) visible satellite image with [the](#) spatial resolution of 50  
 119 m on August 4 [in](#) 2020 to show the organized structures (cellular convection) in  
 120 southeastern TP, [as shown in Figure 1](#). GF 4 is a geostationary earth observation  
 121 satellite in the Gaofen series of Chinese civilian remote sensing satellites. We also use  
 122 the 1 year (from June 1 to August 31 [in](#) 2016) geostationary satellite himawari-8  
 123 retrieval product (cloud top height) over land in East Asia.

124 In this study, [we also use monthly mean we also use](#) temperature (T) [at 2 m](#)  
 125 [height, and](#) relative humidity (RH) at 2 m height, surface pressure, [and](#) planetary  
 126 boundary layer height (PBLH) [every hour](#) from ERA5 reanalysis data from 2010 to  
 127 2019. [To be specific, the above four variables represent hourly average values for](#)  
 128 [each month \(24 values in total for a month\).](#) The lifting condensation level (LCL) is  
 129 calculated by [the](#) method proposed by (Romps, 2017).

130 Using sensible heat flux  $H$ , Northward turbulent surface stress  $\tau_y$  and Eastward  
 131 turbulent surface stress  $\tau_x$  from ERA5 reanalysis data, [then](#) we calculate the  
 132 buoyancy term (BT) ( $g/\theta_v \bar{w}'\theta'_v$ ) and shear term (ST) ( $-\bar{\partial u}/\partial z \bar{u}'\bar{w}'$ ) in the TKE  
 133 equation for each grid. Both of these two terms can be used to analyze the effect of  
 134 boundary layer turbulence in surface layer on convection. The details of the method  
 135 for computing BT and ST are as follows:

136 The shear term (ST) ( $-\bar{\partial u}/\partial z \bar{u}'\bar{w}' - \bar{\partial v}/\partial z \bar{v}'\bar{w}'$ ) and buoyancy term (BT) ( $g/\theta_v \bar{w}'\theta'_v$ )  
 137 in the TKE equation maintain the turbulent motions. In order to simplify calculations,  
 138 the x-axis is directed along the average wind. Assuming horizontal homogeneity and  
 139 no mean divergence, the TKE equation is written as

$$140 \quad \frac{\partial \bar{e}}{\partial t} = \frac{g}{\theta_v} \bar{w}'\theta'_v - \bar{u}'\bar{w}' \frac{\partial \bar{u}}{\partial z} - \frac{\partial(\bar{w}'\bar{e})}{\partial z} - \frac{1}{\rho} \frac{\partial(\bar{w}'\bar{p}')}{\partial z} - \varepsilon. \quad (1)$$

141 The left side of eq. (1) is the local time variation  $\partial \bar{e}/\partial t$ , and the terms on the  
 142 right-hand side of eq. (1) describe the buoyancy and shear energy production or  
 143 consumption, turbulent transport of  $\bar{e}$ , pressure correlation and viscous dissipation  
 144 (Stull, 1988).

145 Here we use eq. (2) to calculate [the](#) virtual potential temperature  $\theta_v$ , and  $\bar{w}'\theta'_v$  is  
 146 derived from eq. (3). Finally, we derive BT.

$$147 \quad \theta_v = T \left(1 + 0.608q\right) \left(\frac{p_0}{p}\right)^{\frac{R}{c_p}}, \quad (2)$$

$$148 \quad H = \rho c_p \bar{w}'\theta'_v, \quad (3)$$

149 Where  $g = 9.8 \text{ m s}^{-2}$  is the gravitational constant, and  $H (\text{W m}^{-2})$  is the sensible heat  
 150 flux,  $\rho (\text{kg m}^{-3})$  is the air density,  $R$  is the specific gas constant for dry air,  $c_p (=1004 \text{ J}$   
 151  $\text{kg}^{-1} \text{ K}^{-1})$  is the specific heat of air at constant pressure,  $T$  is the air temperature at 2 m

height,  $q$  is the specific humidity at 2 m height,  $p_0$  and  $p$  are standard atmospheric pressure and surface pressure, respectively.

For ERA5 reanalyze data, the  $\bar{\partial u}/\partial z$  in the surface layer is estimated as

$$\frac{\bar{\partial u}}{\partial z} = \phi_m(\zeta) \frac{u_*}{kz}, \quad (4)$$

and the (i) Unstable conditions ( $\zeta = z/L < 0$ ). The non-dimensional wind profiles  $\phi_m$  are deduced from eq.(5), as proposed by (Dyer, 1974) is:

$$\phi_m = (1 - 16\zeta)^{-1/4}, (\zeta < 0) \quad (5)$$

(ii) Stable conditions ( $\zeta = z/L > 0$ ). The stable profile functions are assumed to have the empirical forms proposed by Holtslag and Bruun (1988). The universal profile stability functions  $\psi_m$  can be written as

$$\psi_m = -b \left( \zeta - \frac{c}{d} \right) \exp(-d\zeta) - a\zeta - \frac{bc}{d}, \quad (6)$$

Where  $a = 1$ ,  $b = 2=3$ ,  $c = 5$ , and  $d = 0.35$ . Then  $\phi_m$  can be estimated with the help of the relationship  $\phi_m = 1 - \zeta (\partial \psi_m / \partial \zeta)$ .

$$\phi_m = 1 + 5\zeta, (\zeta > 0) \quad (5)$$

$$\phi_m = (1 - 16\zeta)^{-1/4}, (\zeta < 0) \quad (6)$$

$$\zeta = \frac{z}{L}, L = -\frac{(\tau/\rho)^{3/2}}{\kappa(g/\theta_v)(H/\rho c_p)}, \quad (7)$$

$$\tau = \sqrt{\tau_x^2 + \tau_y^2}, \quad (8)$$

$$\tau = \rho u_*^2, \quad (9)$$

$$\tau = -\rho \bar{u} \bar{w}'. \quad (10)$$

Where the von Karman constant  $\kappa = 0.4$ , and  $z = 10$  m.  $\bar{u}$  is the horizontal wind speed at level  $z$  and  $u_*$  is the frictional velocity. The stability parameter  $z/L$  is defined in eq.(7), and the Obukhov length  $L$  can be directly written as a function of  $\tau$  and  $H$  in eq.(7) (Gryanik et al. 2020).  $\tau_x$  and  $\tau_y$  are the Eastward and Northward turbulent surface stress, respectively.  $\tau$  is turbulent fluxes of momentum, which can be

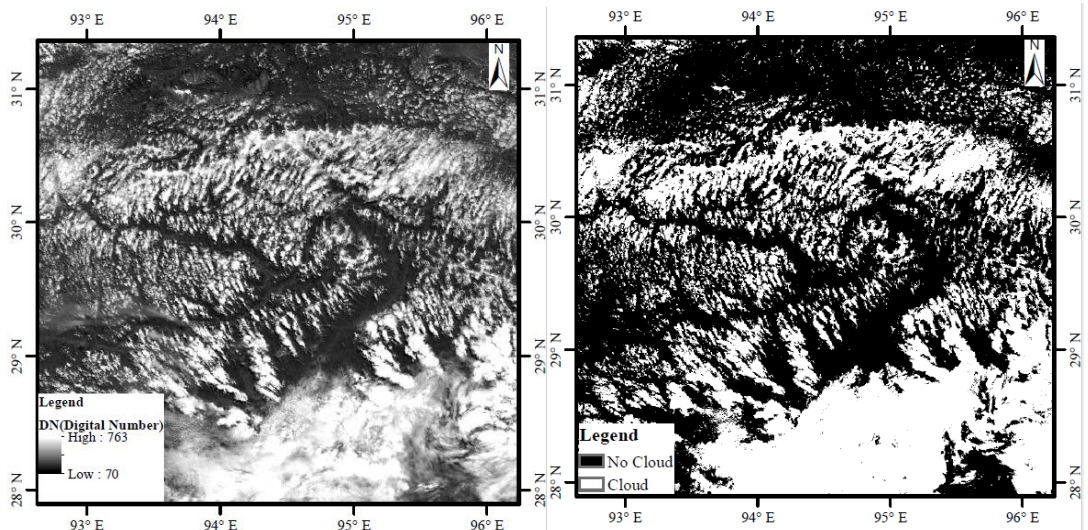
176 calculated by using eq. (8). Then we use eq. (9) to derive  $u_*$ . We also use eq. (10) to  
177 derive  $-\overline{u'w'}$ . Finally, we derive ST.

178

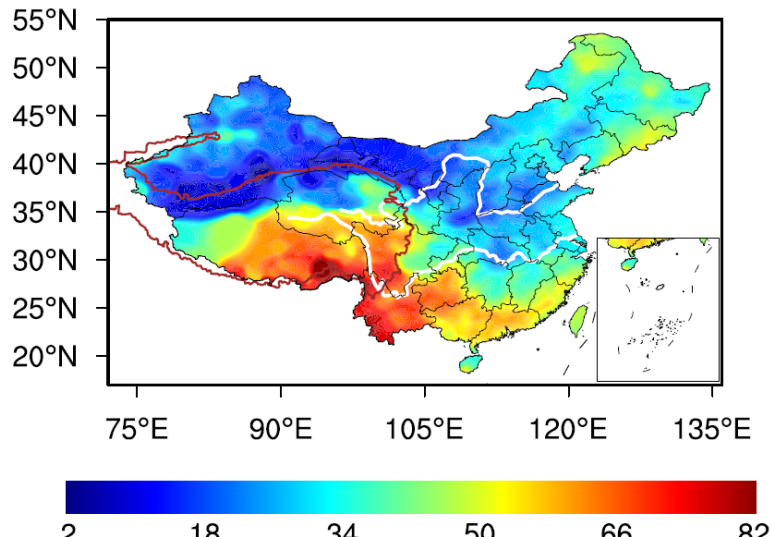
179 **3 Results**

180 Figure 2— shows the spatial distribution of over-land low cloud cover (LCC) in  
181 China from June to August of 1951-2019. Compared to the low LCC in eastern China,  
182 the high value areas of LCC are mainly located in the mid-eastern TP and the area of  
183 the upper Yangtze River Valley. But there are low LCC is also identified in western  
184 and northern parts of TP, w. We will make a further discuss about it in subsequent  
185 paragraphs. Using four years of CloudSat-Calipso satellite data, Li and Zhang (2016)  
186 also—confirmed that the climatological occurrence of cumulus over the TP is  
187 significantly greater than that in mid-eastern China on the same latitude. The elevated  
188 land surface with strong radiative heating makes the massive TP a favorable region  
189 for initiating convective cells with a high frequency of cumulonimbus and mesoscale  
190 convective systems (Sugimoto and Ueno, 2012). As a strong heat source, the TP has  
191 frequent convective activities in summer. During the TIPEX II in 1998, the long  
192 and narrow thermal plume corresponding with vigorous cellular convection on  
193 micro-scale was observed by sodar in Dangxiong. As shown in Figure 1, the  
194 convective plume and “raised” shallow convective clouds on a horizontal scale from  
195 hundreds of meters to several kilometres over the southeastern TP (92.7-96.2E,  
196 29.5-31.3Nabove latitude 30N) are probably related to the organized eddies on the  
197 meso-scale and micro-scale over the TP. The cloud fraction over the southeastern TP  
198 is about 31.3%.

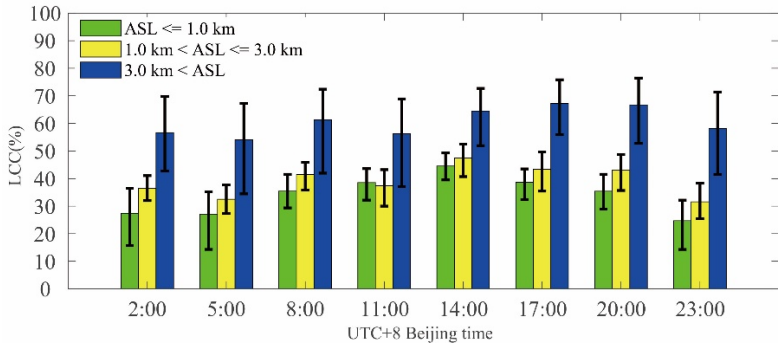
199 As shown in Figure 3, in general, LCC increases with the increasing elevation.  
200 The median of  $LCC_H$  areis significantly greater than those of  $LCC_L$  and  $LCC_M$   
201 throughout the day. The diurnal variations of  $LCC_L$  and  $LCC_M$  are generally  
202 distributed in unimodal pattern, with the maximum appearing at 2:00 pm BT (median  
203  $LCC_L = 37\%$ ,  $LCC_M = 38\%$ ) and low values ( $\sim 20\%$ ) are maintained during the night.  
204 The diurnal variation of  $LCC_H$  presents a bimodal curve with the maximum appearing  
205 at 5:00 pm BT (median  $LCC_H = 69\%$ ) and the secondary local maximum appearing  
206 at 8:00 am BT (median  $LCC_H = 61\%$ ). Compared to the low elevation, the interquartile  
207 ranges (IQRs) of  $LCC_H$  are lesssmaller than those of  $LCC_L$  and  $LCC_M$ , which imply  
208 the  $LCC_H$  maintains high values during the day. To further confirm and compare the  
209 above results fromwith in situ measurements, using ERA5 LCC data, we also add  
210 Figure S1 to show the diurnal cycle of LCC in summer in East Asia and North  
211 America in the supplementary material.



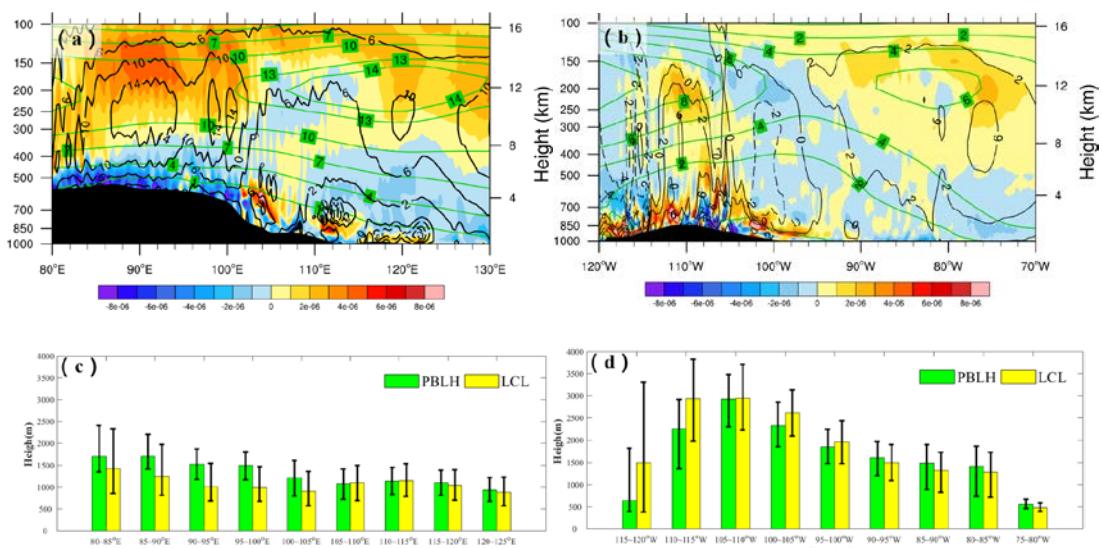
212  
213      Figure 1. The (a) digital number (DN), and (b) spatial distribution of cloud in  
214      southeastern TP from geostationary earth observation satellite Gaofen 4 (GF4) at  
215      12:00 pm Beijing time (about 10:20 am local time) on August 4 of 2020 southeastern  
216      TP. Here we simply use  $DN = 250$  as a threshold. All the grids in Figure (a) are  
217      divided into two classes ( $DN > 250$ , cloud;  $DN < 250$ , no cloud), and then we give  
218      Figure (b).



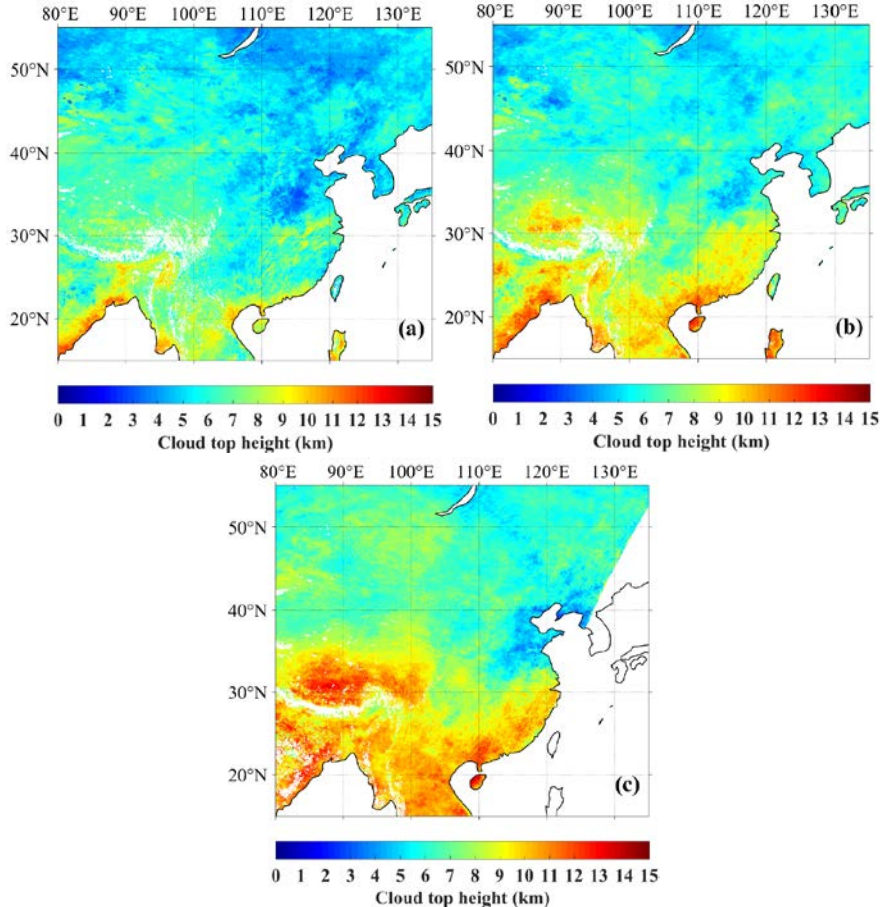
219  
220      Figure 2. The summer mean LCC derived from surface observations in summer from  
221      1951 to 2019 in China. The thick  
222      red contour denotes the 2.5 km topography height referred to as the TP. The white  
223      blue-lines located in northern and southern parts of China denote the Yellow and  
224      Yangtze River, respectively.



225  
226 Figure 3. The diurnal cycle of LCC in summer from 2010 to 2019 at different  
227 altitudes above sea level (ASL): ASL  $\leq$  1.0 km (LCC<sub>L</sub>), 1.0 km  $<$  ASL  $\leq$  3.0 km  
228 (LCC<sub>M</sub>), and 3.0 km  $<$  ASL (LCC<sub>H</sub>). It should be noted that all the sites are ranged  
229 from 27N to 40N in China, and each sample is derived from monthly mean LCC at a  
230 particular time in summer for each site. The bar and error bar represent the median  
231 values and interquartile ranges (IQRs) of LCC, respectively. The subscripts L, M and  
232 H of LCC denote the low, medium and high clouds, respectively.  
233



234  
235 Figure 4. Vertical distribution of divergence ( $s^{-1}$ ) (shaded) at the latitude across  
236 sections from 30N to 35N in (a) East Asia, and (b) North America. The green and  
237 black contours denote the summer mean vectors of U- ( $m s^{-1}$ ) and W- ( $10^{-2} m s^{-1}$ )  
238 wind components at local time 2:00 pm from 2010 to 2019 along 30N–35N with the  
239 zonal circulations, respectively. The solid and dash contour lines represent the  
240 positive and negative values, respectively. The black shaded areas represents  
241 topography. The red and black lines in Figure (c) and (d) denote the LCL and PBLH,  
242 respectively. The shaded colors except black in Figure (c) and (d) represent the  
243 vertical gradients of virtual potential temperature  $d\theta_v/dz$ . The PBLH (green) and LCL  
244 (yellow) versus longitude in (c) East Asia, and (d) North America. The bar and error  
245 bar represent the median values and interquartile ranges (IQRs), respectively.  
246  
247



248

249

250 Figure 5. The median cloud top height derived from himawari-8 retrieval product at  
 251 three Beijing times: (a) 2:30 pm $\pm$ 0.5h (b) 4:30 pm $\pm$ 0.5h (c) 6:30 pm $\pm$ 0.5h from June  
 252 to August in 2016 over land in East Asia. Missing data are shaded in white color.  
 253

254 On the other hand, we note that, compared to eastern China, there is no obvious  
 255 decrease trend for the LCC over the TP from late afternoon to evening as shown in  
 256 Figure 3. Based on the spatial distribution of topography in the Northern Hemisphere  
 257 as shown in Figure 7 (a), it is clear that both the TP (27-40N, 70-105E) and Rocky  
 258 Mountains (27-40N, 103-120W) in North America are two large areas with high  
 259 elevations in mid-latitude regions in the Northern Hemisphere, so here we select these  
 260 two typical large topography regions to analyze the triggering effects of large  
 261 topography and related dynamical structure within the boundary layer on convective  
 262 clouds. The Figure 4 (a) shows In general, there are obvious large scale ascending  
 263 motions from near surface layer to upper troposphere over the TP, which correspond  
 264 with the convergence at 500 hPa and the divergence at 200 hPa, as shown in Figure 4  
 265 (a). Figure 4 (c) shows there are generally deep weak inversion layer (about 2 km with  
 266  $d\theta_v/dz < 3 \text{ K km}^{-1}$ ) and positive PBLH-LCL (~500 m) over the TP, and the median  
 267 and IQR of PBLH are close to those of LCL in East Asia. These results are consistent  
 268 with the conclusions proposed by Xu et al. (2014) and Wang et al. (2020). In contrast,  
 269 Figure 4 (b) shows there are only weak large scale ascending motions from near  
 270 surface layer to middle troposphere over the Rocky Mountains, while and the  
 271 large-scale subsidence on both sides of the Rocky Mountains can leads to strong

inversion above PBL and lower RH in near surface layer. The former restricts the growth of PBLH during the day, andwhile the latter leads to the increased LCL. Thus, negative PBLH-LCL is identified on both sides of the Rocky Mountains (30-35N, 110-120W and 30-35N, 100-105W), especially for the western Rocky Mountain (30-35N, 110-120W) with strong large-scale subsidence, as shown in Figure 4 (d). With its thermal structure, the TP leads to dynamic processes of vapor transport are generated because of the thermal structure of the TP, which is similar to the conditional instability of the second kind (CISK) mechanism of tropical cyclones. It should be pointed out that there are large scale descending motions at 500 hPa in part of western TP and Qaidam Basin as shown in Figure S2, which leads to less LCC in these regions compared to the other parts of the TP, as shown in Figure 2. In addition, the meteorological stations in northern part of TP (34-36N, 80-90E) are scarcely and unevenly distributed, and therefore the low LCC in the Taklamakan Desert leads to fake low LCC values in northern part of TP (80-90E, 34-36N), as shown in Figure 2. In fact, there are high LCC in these regions as shown in Figure 7 (e).

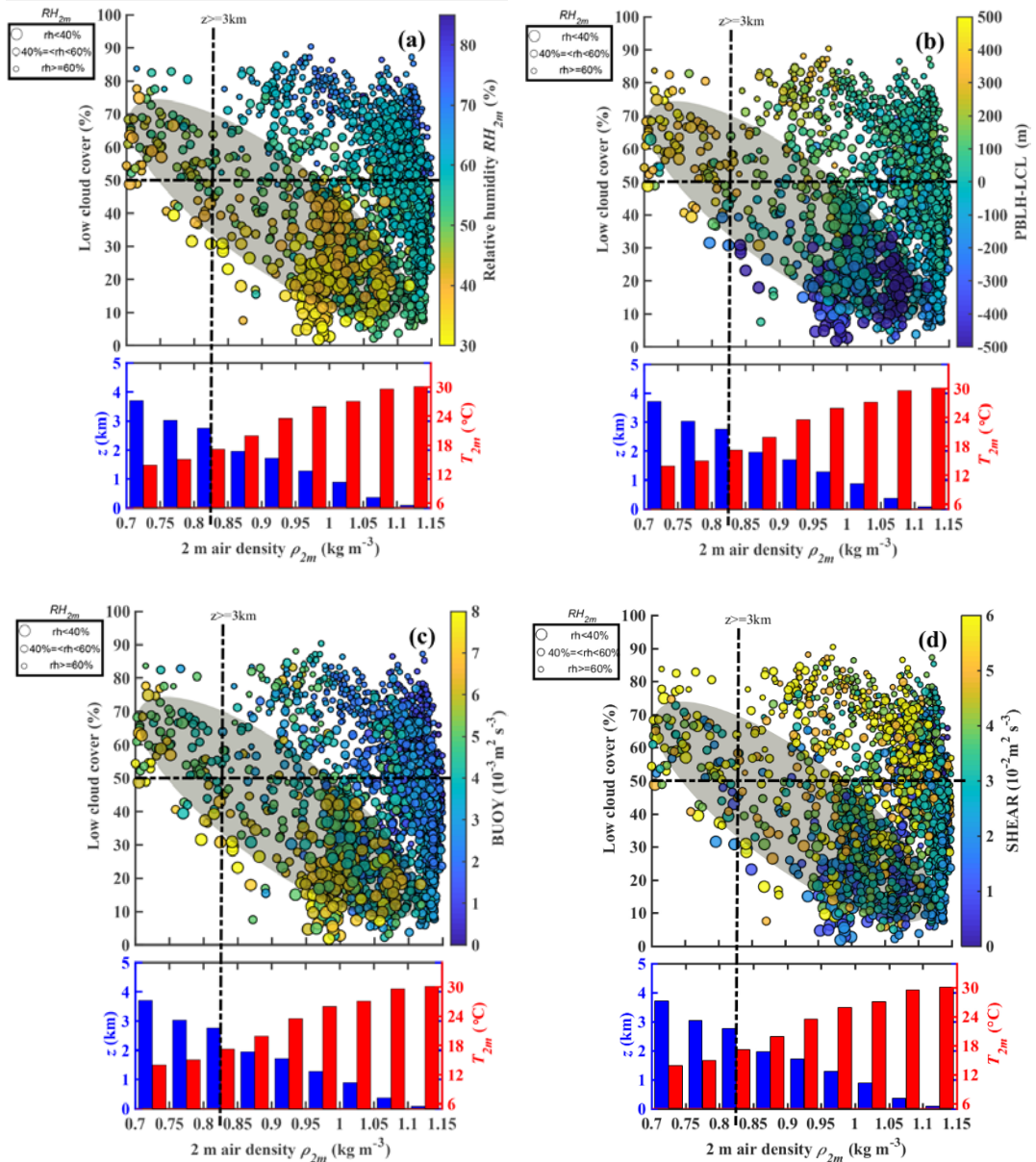
Figure 5 shows the spatial distribution of day time variations of cloud top height in summer. Compared to eastern China at the same latitude, the cloud top height has a significant increase significantly from 2:30 pm (~7 km) to 6:30 pm (~14 km) over the TP. The cloud top height approaches the tropopause (~14 km) in the evening over the TP, which implies the frequent occurrence of deep convective clouds at this time. This result is consistent with the observation of millimeter-wave radar in Naqu (Yi, 2016).

By comprehensively analyzing the second Tibet Plateau Experiment (TIPEX II) sodar data, Xu et al. (2002) and Zhou et al. (2000) found that, with narrow upward motion and time scale from 1.2 h to 1.5 h, the maximum upward motion of the thermal turbulence was identified at the height of about 120 m above the surface, its with the vertical speed up to  $1 \text{ m s}^{-1}$ . They also found symmetrical and wide downward motion area on either side of the narrow upward motion zone. The question arises as to whether there is a relationship between the formation and evolution of frequent "pop-corn-like" convective clouds and micro-scale thermal turbulence in the atmospheric convective boundary layer over the TP. Xu et al., (2012) speculate these low clouds are probably initiated by strong thermal turbulence under low air density conditions. Compared to the low elevation in eastern China, the increased thermal turbulence associated with low air density over the TP leads to the different turbulence characteristics of convective boundary layer (CBL). The CBL is mainly driven by buoyancy heat flux, and the thermal turbulence with organized thermal plume is not totally random (Young, 1988a; Young, 1988b). The BT and ST over the TP are significantly greater than those at the low elevation, which play key roles in the convective activities in lower troposphere.

By using the statistical results from sodar data in the second Tibetan Plateau Experiment for atmospheric sciences (TIPEX II), Zhou et al. (2000) calculated the BT and ST at the height of 50 m under strong convection conditions in Dangxiong (located at central TP). The results indicate that the BT is comparable to ST. Both the thermodynamic and dynamic processes have important influences on the convective

316 activities. Both the BT and ST in the surface layer in Dangxiong are almost an order  
317 of magnitude greater than those at low elevation given by Brummer (1985) in North  
318 Sea and Weckwerth et al. (1997) in Florida. Direct measurements from the Third  
319 Tibetan Plateau Experiments (TIPEX III) also confirmed that surface buoyancy flux  
320 over the TP is significantly larger than that in eastern China (Zhou, 2000; Wang et al.,  
321 2016). Both the sodar data in TIPEX II and boundary layer tower data in TIPEX III  
322 showed contributions of BT and ST to the turbulent kinetic energy in the lower  
323 troposphere are larger over the TP than over the southeastern margin of the TP and the  
324 low-altitude Chengdu Plain (Zhou, 2000; Wang et al., 2015). What is the relationship  
325 between high frequent low cloud and the above physical quantities (e.g. turbulence  
326 structure, temperature and humidity) under low air density conditions over the TP?  
327 The physical mechanism should be discussed and analyzed. In addition, at low  
328 elevation in eastern China, the question arises as to whether or not the variations of  
329 PBLH and LCL favor the formation and development of low clouds.

330 As shown in Figure 6 (a), compared to the low elevation, ~~for low RH<sub>2m</sub> condition~~  
331 (~~RH<sub>2m</sub> < 40%~~), there is larger LCC (LCC > 50%) over the TP (ASL > 3 km) under  
332 low RH<sub>2m</sub> condition (RH<sub>2m</sub> < 40%). In contrast, larger LCC mostly corresponds to  
333 higher RH<sub>2m</sub> condition at low elevation, which is consisted with our common sense.  
334 The above interesting phenomenon can be explained by the differences of PBLH-LCL  
335 between the TP and low elevation on summer afternoons, which are mainly attributed  
336 to two mechanisms. With a similar sensible heat flux, the lower air density over the  
337 TP leads to greater surface buoyancy flux (or BT) as shown in Figure 6 (c), which is  
338 conducive to the increase of ~~PBLH~~ over the TP. Figure 6 (d) shows great ST over  
339 the TP, which is mainly attributed to large wind speed. Although here we only show  
340 the ST in the surface layer, strong wind shear in the boundary layer probably also  
341 plays a role in increasing PBLH over the TP. On the other hand, with a similar RH,  
342 Wang et al. (2020) have indicated that, compared to the low elevation in eastern China,  
343 the lower temperature over the TP leads to a lower LCL. Together these two  
344 mechanisms lead to a greater (PBLH-LCL) difference over the TP on summer  
345 afternoons, which increases the probability of air parcels reaching the LCL and  
346 forming clouds as shown in Figure 6 (b). ~~For the TP, in~~ In most cases, the positive value  
347 of PBLH-LCL, as well as the great BT and ST over the TP corresponds with larger  
348 LCC (LCC > 50%) under low RH<sub>2m</sub> condition (for low RH<sub>2m</sub> < 60%), which implies  
349 the local more enhanced local LCC is relevant to the diurnal variation of the PBL  
350 process. In contrast, for the eastern China, in most cases, the larger increased LCC  
351 (LCC > 50%) generally corresponds with the high RH<sub>2m</sub> (RH<sub>2m</sub> > 60%), and the LCC  
352 is not significantly correlated with PBLH-LCL, or BT and ST, which implies the other  
353 factors besides the PBL process (e.g. large scale ascending motion) play a more  
354 important in LCC.



355

356

357 Figure 6. The relationships among monthly means of low cloud cover LCC,  $\rho_{2m}$  and  
 358 (a)  $RH_{2m}$ , (b) PBLH-LCL, (c) BT and (d) ST at 2:00 pm (BT) from 2010 to 2019 in  
 359 summer in China. The samples are divided into three groups:  $RH_{2m} \geq 60\%$  (small  
 360 size dots),  $60\% > RH_{2m} \geq 40\%$  (median size dots) and  $RH_{2m} < 40\%$  (large size dots).  
 361 The LCC,  $T_{2m}$  and  $RH_{2m}$  are observed by in situ measurements, and PBLH, LCL, BT  
 362 and ST are derived from ERA5 reanalysis data. Here we use the nearest neighbor  
 363 gridding method to derive the PBLH, LCL, BT and ST at each site. The blue and red  
 364 histograms show an approximate relationship between  $\rho_{2m}$  and surface elevation  
 365 above sea level  $z$ , air temperature at 2 m ( $T_{2m}$ ) at the bottom of Figure 2a, respectively.  
 366 The dots with lower  $RH_{2m}$  ( $RH_{2m} < 40\%$ ) are mostly distributed within grey shaded  
 367 elliptic regions as shown in Figure 6 (a)-(d).

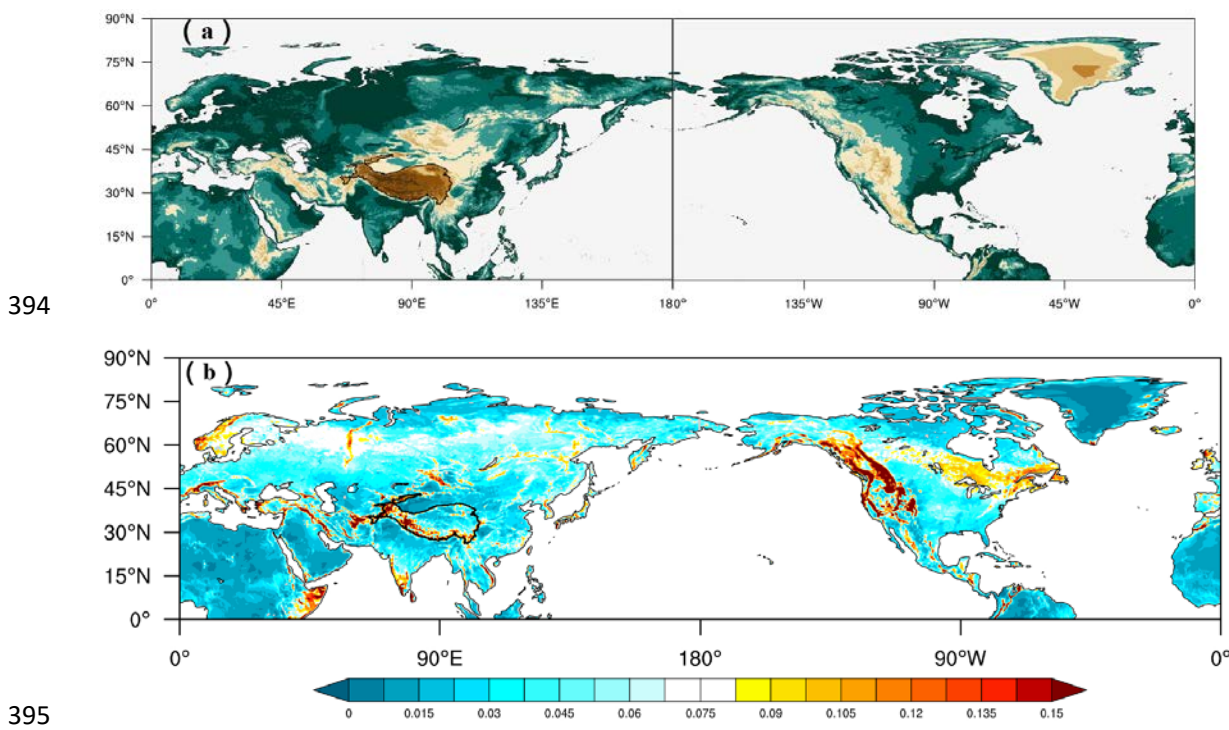
368 Hemisphere Figure 7 (d) shows the mean spatial distribution of PBLH – LCL in  
 369 the Northern Hemisphere from June to August of 2010-2019. The TP (27-40N,  
 370 70-105E) and Rocky Mountains (27-40N, 103-120W) are two typical high value

371 regions in the Northern Hemisphere, and the mean PBLH – LCL over the TP and  
372 Rocky Mountains are 376.7 m and -101.9 m, respectively.

373 Figure 7 (b)-(c) show the spatial distribution of ST and BT in the Northern  
374 Hemisphere from June to August of 2010-2019, respectively. The effect of strong  
375 thermal turbulence results in obvious positive value of PBLH – LCL at high elevation  
376 regions under low air density conditions<sup>3</sup> in the Northern Hemisphere (BT = 0.008 m<sup>2</sup>  
377 s<sup>-3</sup>, PBLH – LCL = 376.7 m over the TP and BT = 0.011 m<sup>2</sup> s<sup>-3</sup>, PBLH – LCL =  
378 -101.9 m over the Rocky Mountains). Figure 7 (b) also shows that there are strong  
379 STs at these two high elevation regions (ST = 0.087 m<sup>2</sup> s<sup>-3</sup> over the TP and ST = 0.085  
380 m<sup>2</sup> s<sup>-3</sup> over the Rocky Mountains). Both the BT and ST increase significantly at high  
381 elevation due to low air density compared to those at low elevation. The above results  
382 enlighten us on thinking about whether the triggering effects of large topography and  
383 boundary layer turbulence, which reflect the special turbulence characteristics in  
384 boundary layer at high elevation regions under low air density conditions<sup>3</sup>, can be  
385 applicable for any large topography in the globe, including TP and other regions (e.g.  
386 Rocky Mountains).

387 Figure 8 shows the conceptual model of atmosphere from the near-surface to  
388 upper troposphere over the TP. Compared to the low elevation, the TP is characterized  
389 by higher PBLH and lower LCL because of strong BT and ST, which is favorable for  
390 the formation of shallow clouds in the afternoon. Meanwhile, the large scale  
391 ascending motion over the TP results in the transition from shallow clouds to deep  
392 convective clouds in the late afternoon and evening.

393



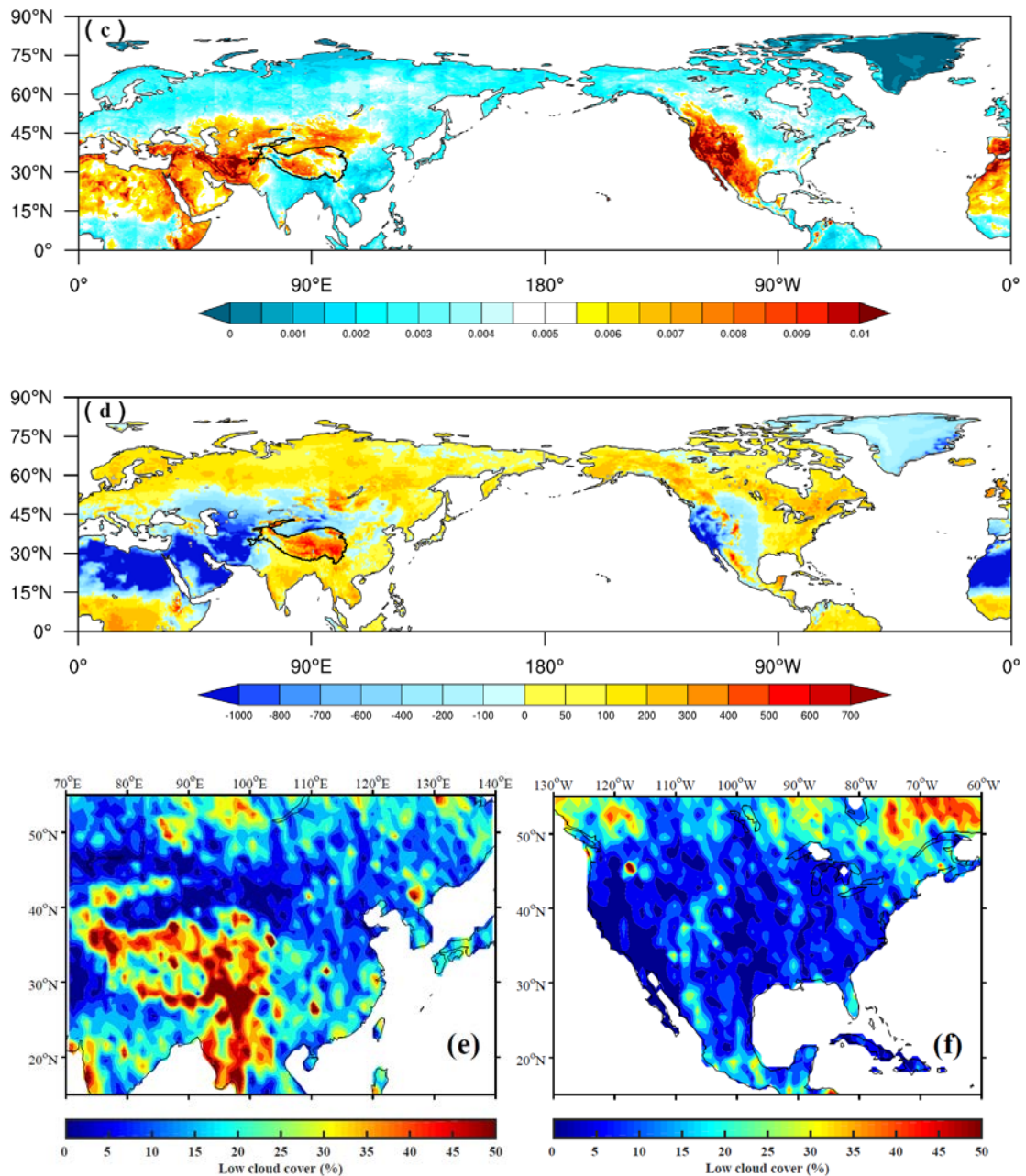
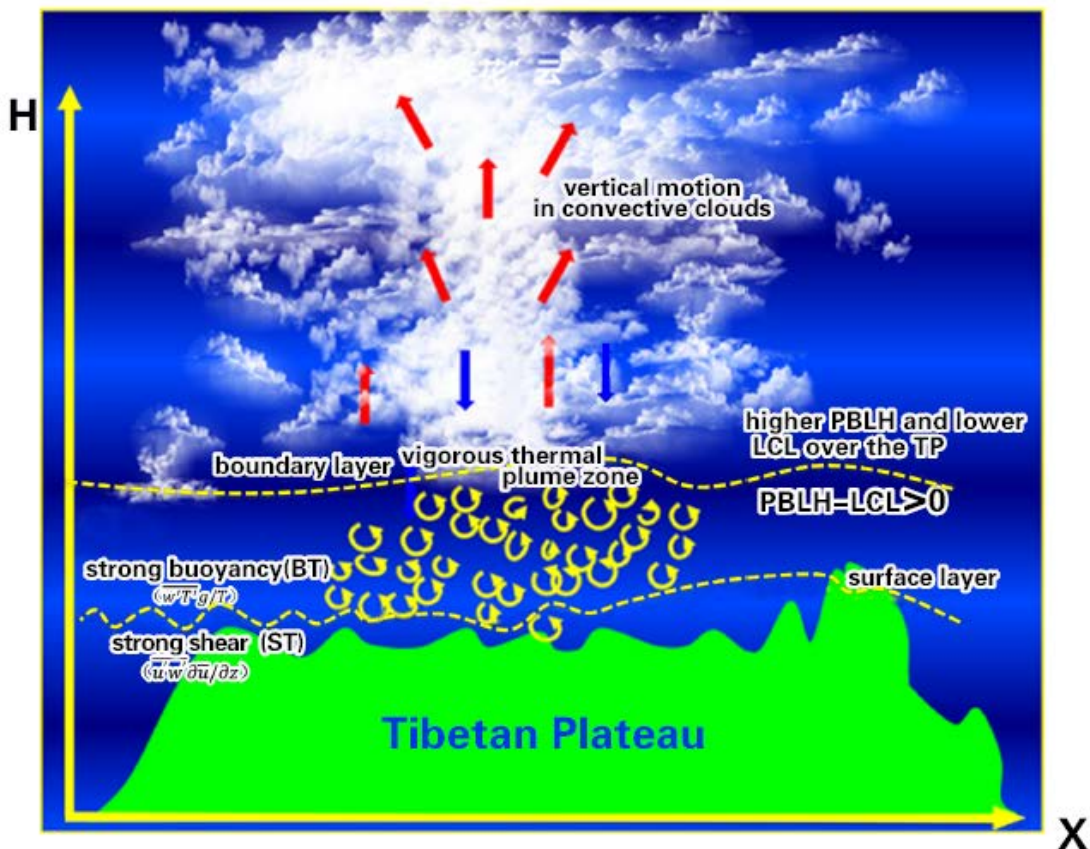


Figure 7. The spatial distribution of (a) ground level elevation, (b) ST, (c) BT, [and](#) (d) PBLH-LCL, and (e) LCC derived from ERA5 reanalysis data at local time 2:00 pm in the Northern Hemisphere in summer. Figure (e) and (f) are the summer mean LCC derived from cloudsat satellite data at local time 2:00 pm in eastern China and North America, respectively.



407

408

409 Figure 8. The characteristics model of boundary layer turbulence related to “high efficiency” triggering mechanisms for convection over the TP.

410 **4 Conclusions and further discussion**

411 In this study, we focus on the triggering effects of large topography and  
 412 boundary layer turbulence over the Tibetan Plateau on convection. The topography of  
 413 the TP also has a major role in the increasing ofincreased occurrences of convective  
 414 clouds. Our results further confirm the conclusions from Wang et al. (2020), which  
 415 found that PBLH-LCL over the TP is greater than that in eastern China. Compared to  
 416 the eastern China, with the same relative humidity, lower temperature over the TP  
 417 results in a lower lifting condensation level. With the same surface sensible heat flux,  
 418 lower air density over the TP results in a larger buoyancy flux and a deeper boundary  
 419 layer. The observational results show that, under low relative humidity condition (RH  
 420 < 40%), the low cloud cover (LCC) is higher than 60% over the TP. In contrast, the  
 421 high LCC (LCC > 60%) only appears under conditions withhigh RH condition (RH >  
 422 60%) at low elevation.

423 In general, LCC increases with the increasing elevation. The median of LCCs at  
 424 high elevation (TP) areis significantly greater than those at low elevation (eastern  
 425 China) throughout the day. The diurnal variations of LCC in eastern China are  
 426 generally distributed in unimodal pattern with the maximum appearing at 2:00 pm BT

427 and— low values during the night. The diurnal variations of LCC at high elevation  
428 (TP) present a bimodal curve with the maximum appearing at 5:00 pm BT and the  
429 secondary local maximum appearing at 8:00 am BT. In addition, LCC maintains at  
430 high values at high elevation (TP) during the day. The median cloud top height  
431 derived from himawari-8 retrieval product shows the transition from shallow clouds  
432 to deep convective clouds in the late afternoon and evening over the TP, which is  
433 attributed to the strong large-scale ascending motion from the near surface to upper  
434 troposphere over the TP.

435 The buoyancy term (BT) and shear term (ST) over the TP are significantly greater  
436 than those at the low elevation, which is favorable for the ~~formation of~~ increasing ~~of~~  
437 PBLH. Similar phenomenon occurs at other high elevation areas (e.g. Rocky  
438 Mountains). The strong thermal turbulence results in positive value of PBLH-LCL at  
439 high elevation regions under low RH condition in the Northern Hemisphere. The  
440 slightly greater than zero ~~PBLH-LCL~~ corresponds spatially to ~~more increased~~ LCC  
441 in the central part of Rocky Mountains, but ~~the~~ obvious large-scale subsidence on  
442 both sides of the mountain leads to strong inversion above PBL and lower RH in PBL,  
443 which further lead to ~~less decreased~~ LCC in these areas. Thus— less LCC is generated  
444 at Rocky Mountains compared to the TP.

445

#### 446 **Data availability**

447 All reanalysis data used in this study were obtained from publicly available sources:  
448 ERA5 reanalysis data can be obtained from the ECMWF public datasets web interface  
449 (<http://apps.ecmwf.int/datasets/>). The satellite (CloudSat radar and Calipso  
450 lidar)-merged cloud classification product 2B-CLDCLASS-lidar were obtained from  
451 Colorado State University  
452 (<http://www.cloudsat.cira.colostate.edu/data-products/level-2b/2b-cldclass-lidar>). The  
453 himawari-8 retrieval products were obtained from JAXA Himawari Monitor  
454 (<https://www.eorc.jaxa.jp/ptree/>).

#### 455 **Code Availability**

456 The data in this study are analysed with MATLAB and NCL. Contact Y.W. for specific  
457 code requests.

#### 458 **Acknowledgements**

459 Xu and Wang are supported by the Second Tibetan Plateau Scientific Expedition and  
460 Research (STEP) program (Grant Nos. 2019QZKK0105), National Natural Science  
461 Foundation of China (Grant Nos. 91837310), and the National Natural Science  
462 Foundation for Young Scientists of China (Grant Nos. 41805006).

463 **Author Contributions**

464 X.X. and Y. W. led this work with contributions from all authors. Y.T. and Y. W.  
465 made the calculations and created the figures. X.X., Y.W. and S.Z. led analyses,  
466 interpreted results and wrote the paper.

467 **Competing interests**

468 The authors declare no competing interests.

469

470 **References**

471 Brümmer, B.: Structure, dynamics and energetics of boundary layer rolls from Kon  
472 Tur aircraft observations, undefined, 1985.

473 Dyer, A. J.: A review of flux-profile relationships, *Bound.-Layer Meteorol.*, 7, 363–  
474 372, <https://doi.org/10.1007/bf00240838>, 1974.

475 Ek, M. and Mahrt, L.: Daytime Evolution of Relative Humidity at the Boundary  
476 Layer Top, *Mon. Weather Rev.*, 122, 2709–2721,  
477 [https://doi.org/10.1175/1520-0493\(1994\)122<2709:DEORHA>2.0.CO;2](https://doi.org/10.1175/1520-0493(1994)122<2709:DEORHA>2.0.CO;2), 1994.

478 Findell, K. L. and Eltahir, E. A. B.: Atmospheric Controls on Soil Moisture–Boundary  
479 Layer Interactions. Part I: Framework Development, *J. Hydrometeorol.*, 4, 552–569,  
480 [https://doi.org/10.1175/1525-7541\(2003\)004<0552:ACOSML>2.0.CO;2](https://doi.org/10.1175/1525-7541(2003)004<0552:ACOSML>2.0.CO;2), 2003.

481 Flohn, H. and Reiter, E. R.: Contributions to a meteorology of the Tibetan highlands,  
482 1967.

483 Holtslag, A. A. M. and Bruin, H. A. R. D.: Applied modelling of the night-time  
484 surface energy balance over land. *J. Appl. Meteorol.*, 27, 689–704. doi:  
485 [10.1175/1520-0450\(1988\)027<0689:AMOTNS>2.0.CO;2](https://doi.org/10.1175/1520-0450(1988)027<0689:AMOTNS>2.0.CO;2), 1988.

486 Gentine, P., Holtslag, A. A. M., D'Andrea, F., and Ek, M.: Surface and Atmospheric  
487 Controls on the Onset of Moist Convection over Land, *J. Hydrometeorol.*, 14, 1443–  
488 1462, <https://doi.org/10.1175/JHM-D-12-0137.1>, 2013.

489 Gryanić, V. M., Lüpkes, C., Grachev, A., & Sidorenko, D.: New modified and  
490 extended stability functions for the stable boundary layer based on SHEBA and  
491 parametrizations of bulk transfer coefficients for climate models. *J. Atmos. Sci.*, 77(8),  
492 2687–2716, <https://doi.org/10.1175/JAS-D-19-0255.1>, 2020.

493 Guillod, B. P., Orlowsky, B., Miralles, D. G., Teuling, A. J., and Seneviratne, S. I.:  
494 Reconciling spatial and temporal soil moisture effects on afternoon rainfall, *Nat.*  
495 *Commun.*, 6, 6443, <https://doi.org/10.1038/ncomms7443>, 2015.

496 Hersbach, H., Bell, B., Berrisford, P., Hirahara, S., Horányi, A., Muñoz-Sabater, J.,  
497 Nicolas, J., Peubey, C., Radu, R., Schepers, D., Simmons, A., Soci, C., Abdalla, S.,  
498 Abellan, X., Balsamo, G., Bechtold, P., Biavati, G., Bidlot, J., Bonavita, M., Chiara, G.

499 D., Dahlgren, P., Dee, D., Diamantakis, M., Dragani, R., Flemming, J., Forbes, R.,  
500 Fuentes, M., Geer, A., Haimberger, L., Healy, S., Hogan, R. J., Hólm, E., Janisková,  
501 M., Keeley, S., Laloyaux, P., Lopez, P., Lupu, C., Radnoti, G., Rosnay, P. de, Rozum,  
502 I., Vamborg, F., Villaume, S., and Thépaut, J.-N.: The ERA5 global reanalysis, *Q. J. R.*  
503 *Meteorol. Soc.*, 146, 1999–2049, <https://doi.org/10.1002/qj.3803>, 2020.

504 Li, Y. and Zhang, M.: Cumulus over the Tibetan Plateau in the Summer Based on  
505 CloudSat–CALIPSO Data, *J. Clim.*, 29, 1219–1230,  
506 <https://doi.org/10.1175/JCLI-D-15-0492.1>, 2016.

507 Luo, Y., Zhang, R., Qian, W., Luo, Z., and Hu, X.: Intercomparison of Deep  
508 Convection over the Tibetan Plateau–Asian Monsoon Region and Subtropical North  
509 America in Boreal Summer Using CloudSat/CALIPSO Data, *J. Clim.*, 24, 2164–2177,  
510 <https://doi.org/10.1175/2010JCLI4032.1>, 2011.

511 Romps, D. M. (2017). Exact expression for the lifting condensation level. *Journal of*  
512 *the Atmospheric Sciences*, 74, 3891–3900. <https://doi.org/10.1175/JAS-D-17-0102.1>

514 Sassen, K. and Wang, Z.: Classifying clouds around the globe with the CloudSat radar:  
515 1-year of results, *Geophys. Res. Lett.*, 35, <https://doi.org/10.1029/2007GL032591>,  
516 2008.

517 Stull, R. B.: Mean Boundary Layer Characteristics, in: *An Introduction to Boundary*  
518 *Layer Meteorology*, edited by: Stull, R. B., Springer Netherlands, Dordrecht, 1–27,  
519 [https://doi.org/10.1007/978-94-009-3027-8\\_1](https://doi.org/10.1007/978-94-009-3027-8_1), 1988.

520 Sugimoto, S. and Ueno, K.: Role of Mesoscale Convective Systems Developed  
521 around the Eastern Tibetan Plateau in the Eastward Expansion of an Upper  
522 Tropospheric High during the Monsoon Season, *J. Meteorol. Soc. Jpn. Ser II*, 90,  
523 297–310, <https://doi.org/10.2151/jmsj.2012-209>, 2012.

524 Taylor, C. M., de Jeu, R. A. M., Guichard, F., Harris, P. P., and Dorigo, W. A.:  
525 Afternoon rain more likely over drier soils, *Nature*, 489, 423–426,  
526 <https://doi.org/10.1038/nature11377>, 2012.

527 Tuttle, S. and Salvucci, G.: Empirical evidence of contrasting soil moisture–  
528 precipitation feedbacks across the United States, *Science*, 352, 825–828,  
529 <https://doi.org/10.1126/science.aaa7185>, 2016.

530 Wang, Y., Xu, X., Zhao, T., Sun, J., Yao, W., and Zhou, M.: Structures of convection  
531 and turbulent kinetic energy in boundary layer over the southeastern edge of the  
532 Tibetan Plateau, *Sci. China Earth Sci.*, 58, 1198–1209,  
533 <https://doi.org/10.1007/s11430-015-5054-1>, 2015.

534 Wang, Y., Xu, X., Liu, H., Li, Y., Li, Y., Hu, Z., Gao, X., Ma, Y., Sun, J., Lenschow, D.  
535 H., Zhong, S., Zhou, M., Bian, X., and Zhao, P.: Analysis of land surface parameters

536 and turbulence characteristics over the Tibetan Plateau and surrounding region, *J.  
537 Geophys. Res. Atmospheres*, 121, 9540–9560, <https://doi.org/10.1002/2016JD025401>,  
538 2016.

539 Wang, Y., Zeng, X., Xu, X., Welty, J., Lenschow, D. H., Zhou, M., and Zhao, Y.: Why  
540 Are There More Summer Afternoon Low Clouds Over the Tibetan Plateau Compared  
541 to Eastern China?, *Geophys. Res. Lett.*, 47, e2020GL089665,  
542 <https://doi.org/10.1029/2020GL089665>, 2020.

543 Weckwerth, T. M., Wilson, J., Wakimoto, R., and Crook, N. A.: Horizontal convective  
544 rolls: Determining the environmental conditions supporting their existence and  
545 characteristics, *Mon. Weather Rev.*, 125, 505–526,  
546 [https://doi.org/10.1175/1520-0493\(1997\)12560;0505:hcrdte62;2.0.co;2](https://doi.org/10.1175/1520-0493(1997)12560;0505:hcrdte62;2.0.co;2), 1997.

547 Wu, G., Duan, A., Liu, Y., Mao, J., Ren, R., Bao, Q., He, B., Liu, B., and Hu, W.:  
548 Tibetan Plateau climate dynamics: recent research progress and outlook, *Natl. Sci.  
549 Rev.*, 2, 100–116, <https://doi.org/10.1093/nsr/nwu045>, 2015.

550 Xu, X., Zhou, M., Chen, J., Bian, L., Zhang, G., Liu, H., Li, S., Zhang, H., Zhao, Y.,  
551 Suolongduoji, and Jizhi, W.: A comprehensive physical pattern of land-air dynamic  
552 and thermal structure on the Qinghai-Xizang Plateau, *Sci. China Ser. D*, 45, 577–594,  
553 <https://doi.org/10.1360/02yd9060>, 2002.

554 Xu, X., Zhang, R., Koike, T., Lu, C., Shi, X., Zhang, S., Bian, L., Cheng, X., Li, P.,  
555 and Ding, G.: A New Integrated Observational System Over the Tibetan Plateau, *Bull.  
556 Am. Meteorol. Soc. - BULL AMER METEOROL SOC*, 89, 1492–1496,  
557 <https://doi.org/10.1175/2008BAMS2557.1>, 2008.

558 Xu, X., Shi, X., and Lu, C.: Theory and application for warning and prediction of  
559 disastrous weather downstream from the Tibetan Plateau, *Theory Appl. Warn. Predict.  
560 Disastrous Weather Downstr. Tibet. Plateau*, 1–116, 2012.

561 Xu, X., Zhao, T., Lu, C., Guo, Y., Chen, B., Liu, R., Li, Y., and Shi, X.: An important  
562 mechanism sustaining the atmospheric “water tower” over the Tibetan Plateau,  
563 *Atmospheric Chem. Phys.*, 14, 11287–11295,  
564 <https://doi.org/10.5194/acp-14-11287-2014>, 2014.

565 Yi, C., and Guo, X.: Characteristics of convective cloud and precipitation during  
566 summer time at Naqu over Tibetan Plateau (in Chinese), *Chinese Science Bulletin*, 61,  
567 1706–471, <https://doi.org/10.1360/N972015-01292>, 2016.

568 Young, G. S.: Convection in the atmospheric boundary layer, *Earth-Sci. Rev.*, 25,  
569 179–198, [https://doi.org/10.1016/0012-8252\(88\)90020-7](https://doi.org/10.1016/0012-8252(88)90020-7), 1988a.

570 Young, G. S.: Turbulence Structure of the Convective Boundary Layer. Part I.  
571 Variability of Normalized Turbulence Statistics, *J. Atmospheric Sci.*, 45, 719–726,  
572 [https://doi.org/10.1175/1520-0469\(1988\)045<0719:TSOTCB>2.0.CO;2](https://doi.org/10.1175/1520-0469(1988)045<0719:TSOTCB>2.0.CO;2), 1988b.

573 Zhou, M., Xu, X., Bian, L., Chen, J., Liu H., Zhang, H., Li, S., and Zhao J.:  
574 Observational analysis and dynamic study of atmospheric boundary layer on Tibetan  
575 Plateau (in Chinese), 125 pp., 2000.

576